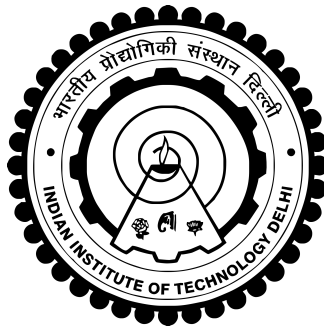

Emergent fractality in graphene-based twisted van der Waals heterostructures

DEEPANSHU AGGARWAL



DEPARTMENT OF PHYSICS
INDIAN INSTITUTE OF TECHNOLOGY DELHI
JULY 2025

© Indian Institute of Technology Delhi (IITD), Delhi, 2025

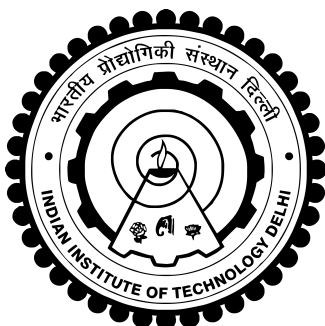
EMERGENT FRACTALITY IN GRAPHENE-BASED TWISTED VAN DER WAALS HETEROSTRUCTURES

by

DEEPANSHU AGGARWAL

Department of Physics

*Submitted in fulfilment of requirements of degree of
Doctor of Philosophy
to the*

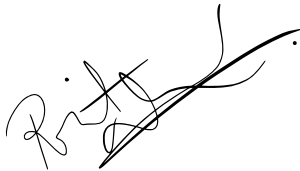


INDIAN INSTITUTE OF TECHNOLOGY DELHI
JULY 2025

Dedicated to my family ...

CERTIFICATE

This is to certify that the thesis entitled “**Emergent fractality in graphene-based twisted van der Waals heterostructures**”, being submitted by **Mr. Deepanshu Aggarwal** to the Department of Physics, Indian Institute of Technology Delhi, for the award of the degree of **Doctor of Philosophy**, is a record of bonafide work carried out by him under our supervision and guidance. The results reported in this thesis have not been submitted, either in part or in full, to any other University or Institute for the award of any degree or diploma.



Prof. Rohit Narula

(Thesis Supervisor)

Department of Physics

Indian Institute of Technology Delhi

Delhi-110016, India



Prof. Sankalpa Ghosh

(Thesis Supervisor)

Department of Physics

Indian Institute of Technology Delhi

Delhi-110016, India

Date : 28th July 2025

ACKNOWLEDGEMENTS

The successful completion of this work is largely due to the support and guidance of many individuals whose valuable contributions greatly enhanced my understanding of the subject matter.

First and foremost, I would like to express my deepest gratitude to my supervisors, Dr. Rohit Narula and Dr. Sankalpa Ghosh, for their invaluable support, guidance, and encouragement throughout my PhD journey. Their profound knowledge, insightful feedback, and never-ending patience have been instrumental in shaping my academic development. I am truly grateful for the opportunities and mentorship they provided, which have not only enriched my academic experience but also my personal growth. Apart from the formal academic discussions, I would also appreciate the informal lunch and coffee sessions they organized to provide a healthy and informal discussion environment among all the members of the research group regarding various topics. This thesis would not have been possible without their constant support and belief in my abilities.

I extend my gratitude to Dr. A.K. Shukla (previous SRC chairman), Dr. D. Bhowmik (previous SRC member), Dr. Sujeet Chowdhary (SRC chairman), Dr. Sujit Manna, and Dr. Nirat Ray, who served as my SRC members and consistently reviewed my work and provided valuable suggestions throughout.

My heartfelt thanks to my seniors, Dr. Manisha Arora, Dr. Inderpreet Kaur, Dr. Poornima Shakya, and Dr. Shahrukh Salim, for providing their valuable guidance whenever needed.

I would like to sincerely thank Dr. Disha Arora, my good friend and collaborator. Her constant encouragement and support have been invaluable throughout this journey. The late-night discussions and shared laughter have made this experience truly remarkable.

I am grateful to my other labmates and colleagues, Mr. Partha Sarathi, Ms. Neha, Ms. Komal, and Ms. Aakanksha, for their unwavering assistance and support. I also cherish the late-night tea time, spontaneous dinner outings, gossip sessions, and unplanned trips with them. My best wishes to all of you.

My five years of hostel life would not have been nearly as enjoyable without the companionship of my friends Manoj, Rakesh, Anuj, Avijit, Om Prakash, Arun, Ketan, Sidharth, and Suvom. Their presence created a lively and enjoyable environment throughout this journey.

Furthermore, I am grateful for the financial assistance provided for my research project, funded by PhD fellowship program from the University Grants Commission (UGC), Government of India.

Without the assistance of my parents, Mrs. Anju and the late Sh. Sanjay Kumar Aggarwal, this journey would not have been feasible. My success has been largely attributed to their belief in me and unwavering patience with me at the lowest points in my life. I am particularly appreciative of my younger sister, Preeti, who has been more of a friend than a sibling and has never stopped encouraging me at different times. I also appreciate my school friend Aakash, who has been a constant source of motivation and has been more like a brother to me.

Finally, I want to express my gratitude and thanks to God, the Almighty, for providing me with innumerable blessings, opportunities, and knowledge that have allowed me to complete the thesis.

A handwritten signature in black ink, appearing to read 'D. A.', with a horizontal line underneath.

Deepanshu Aggarwal

Place: Delhi

ABSTRACT

Van der Waals heterostructures attracted a huge interest towards the exploration of various theoretical and experimental possibilities due to their promising tunable electronic properties. Notably, many strongly correlated phases ranging from Mott insulator to high- T_c superconductivity have been observed in two-dimensional graphene-based materials such as twisted bilayer graphene (tBLG). These correlation-driven phases result due to the non-triviality of the band structure with a strong dependence on the moiré superlattice potential. This thesis explores the complex realm of moiré patterns, a phenomenon resulting from the alignment of two layers due to twist angles and lattice inconsistencies. Exposing the tBLG to a sequence of commensurate external periodic potentials exhibits an emergent fractality, and the self-similarity of the hierarchical structures of Brillouin zones leads to a nested subband configuration inside the bandwidth of the original moiré bands, subsequently enabling a reliable low-energy band count. Furthermore, in the case of multilayer supermoiré (SM) structures created by the superposition of two or more moiré patterns from different interfaces, we demonstrate that these structures exhibit emergent fractality under specific conditions within a comprehensive low-energy framework. Mainly, through the study of hexagonal trilayer and quadlayer SM and considering that the two moiré from distinct interfaces are commensurate with each other, we derived a dominant SM length scale that is determined by the twist angles and lattice mismatches between the layers. Furthermore, we show the single-particle electronic properties along an infinitely countable set of points within a parameter space \mathbb{R}^2 formed by the twist-angles in two interfaces (θ_1, θ_2) . To validate these theoretical predictions, we theoretically analyze modern spectroscopic techniques such as nano angle-resolved photoemission spectroscopy (nano-ARPES) intensity and the tunneling current in scanning tunneling microscopy to verify the band count and emergent fractality by using the single-particle states of the effective Hamiltonian of SM structures to obtain the momentum-space distribution of APRES intensity and local density of states for tunnelling current.

वैन डेर वाल्स हेटेरोस्ट्रक्चर्स ने अपने आशाजनक ट्यूनेबल इलेक्ट्रॉनिक गुणों के कारण विभिन्न सैद्धांतिक और प्रयोगात्मक संभावनाओं के अन्वेषण की ओर भारी रुचि आकर्षित की। विशेष रूप से, ट्विस्टेड बाईलेयर ग्राफीन (टीबीएलजी) जैसी द्वि-आयामी ग्राफीन-आधारित सामग्रियों में मोट इंसुलेटर से लेकर उच्च- T_c सुपरकंडक्टिविटी तक कई दृढ़ता से सहसंबद्ध चरणों को देखा गया है। इन सहसंबंध-संचालित चरणों का परिणाम बैंड संरचना की गैर-तुच्छता के कारण होता है, जिसमें मोयर सुपरलैटिस क्षमता पर मजबूत निर्भरता होती है। यह थीसिस मोयर पैटर्न के जटिल क्षेत्र की पड़ताल करता है, जो मोड़ कोणों और जाली की विसंगतियों के कारण दो परतों के संरेखण के परिणामस्वरूप एक घटना है। टी. बी. एल. जी. को अनुरूप बाहरी आवधिक क्षमताओं के अनुक्रम में उजागर करना एक उभरती हुई अस्थिभंगता को प्रदर्शित करता है, और ब्रिलौइन क्षेत्रों की पदानुक्रमित संरचनाओं की आत्म-समानता मूल मोयर बैंड की बैंडविड्थ के अंदर एक नेस्टेड सबबैंड कॉन्फिगरेशन की ओर ले जाती है, जो बाद में एक विश्वसनीय कम-ऊर्जा बैंड गिनती को सक्षम करती है। इसके अलावा, विभिन्न इंटरफेस से दो या दो से अधिक मोयर पैटर्न के सुपरपोजिशन द्वारा बनाई गई बहुस्तरीय सुपरमॉयर (एसएम) संरचनाओं के मामले में, हम प्रदर्शित करते हैं कि ये संरचनाएं एक व्यापक कम-ऊर्जा ढांचे के भीतर विशिष्ट परिस्थितियों में उभरती फ्रैक्टलिटी प्रदर्शित करती हैं। मुख्य रूप से, षट्कोणीय त्रि-परत और चतुर्भुज-परत एसएम के अध्ययन के माध्यम से और यह देखते हुए कि अलग-अलग इंटरफेस से दो मोयर एक-दूसरे के अनुरूप हैं, हमने एक प्रमुख एसएम लंबाई स्केल प्राप्त किया जो परतों के बीच मोड़ कोण और जाली बेमेल द्वारा निर्धारित किया जाता है। इसके अलावा, हम दो इंटरफेस (θ_1, θ_2) में ट्विस्ट-एंगल द्वारा बनाए गए पैरामीटर स्पेस \mathbb{R}^2 के भीतर अनंत रूप से गणना योग्य बिंदुओं के सेट के साथ एकल-कण इलेक्ट्रॉनिक गुणों को दिखाते हैं। इन सैद्धांतिक भविष्यवाणियों को मान्य करने के लिए, हम सैद्धांतिक रूप से आधुनिक स्पेक्ट्रोस्कोपिक तकनीक जैसे नैनो-एंगल-रिज़ॉल्व्ड फोटोमिशन स्पेक्ट्रोस्कोपी (एआरपीईएस) की तीव्रता और स्कैनिंग टनलिंग माइक्रोस्कोपी में टनलिंग करंट का विश्लेषण करते हैं ताकि बैंड की गिनती और एसएम संरचनाओं के प्रभावी हैमिल्टनियन की एकल-कण अवस्थाओं का उपयोग करके उभरते फ्रैक्टलिटी को सत्यापित किया जा सके।

CONTENTS

Certificate	i
Acknowledgements	ii
Abstract	iv
Table Of Contents	vi
List Of Figures	ix
List Of Tables	xx
List of Symbols	xx
List of acronyms/abbreviations	xxii
1 Introduction	1
1.1 Motivation	1
1.2 Summary of the problems addressed	6
1.3 Organization of the thesis	8
2 A primer on moiré superlattices	11
2.1 Weak correlations to strong correlations in Dirac systems	13
2.1.1 Honeycomb lattice	17
2.1.2 Van Hove singularity (VHS)	22
2.1.3 Graphene under external periodic potentials	24
2.2 Van der Waals heterostructures (a tool for building strong correlations in Dirac systems)	34
2.2.1 Moiré SLs	35
2.2.2 Graphene on hexagonal boron nitride (G/BN)	36
2.3 Twisted Bilayer Graphene	39
2.3.1 Commensurate twisted bilayer graphene	40
2.3.2 The continuum model by Santos <i>et al.</i> [7]	46
2.3.3 Incommensurate structures: a general theoretical framework for interlayer interaction	53
2.4 Bistritzer-MacDonald (BM) model	57
2.4.1 Effective two-bands model	62
2.5 Perfectly flat bands	65

2.5.1	The origin of magic angles [190]	68
2.6	Extended Hamiltonian of TBLG [102]	72
3	Moiré fractals in twisted graphene layers	75
3.1	The Hamiltonian and emergent fractality in moiré fractals	77
3.2	Implications of the above construction for the band structure	80
3.3	Chapter summary	83
4	Commensuration in hBN-encapsulated supermoiré structures and its connection with moiré fractal	86
4.1	Methods	87
4.1.1	Parameter-space of supermoiré systems	87
4.1.2	Band structure calculation and emergence of fractality in an hBN-encapsulated in mono and bilayer graphene systems	90
4.2	Results and Discussion	92
4.2.1	Angle-resolved photoemission spectroscopy (ARPES) to study the emergent fractality in SMS structures	92
4.2.2	Calculation of the differential conductivity in the scanning tunneling microscopic images	95
4.3	Chapter summary	97
5	Conclusions and possible extensions	99
5.1	Future scope	103
5.2	Topics not covered in the chapter-2	104
	Bibliography	109
	Appendix	143
A	A primer on moiré superlattices	143
A.1	Simplification of the term in velocity renormalization	143
A.2	The alternative form of Hamiltonian in BM model	145
B	Moiré fractals in twisted graphene layers	150
B.1	The properties of the fractal generators (FG)	150
B.2	The real-space construction of the moiré fractals	152
B.3	The relation of the number of bands with the fractal dimension (D_f)	152
B.4	Derivation of Eq. (3) of the chapter-3	153
B.4.1	Fractal dimension (D_f) in the metric space of p_1, p_2	154
B.5	More on the incommensuration measure	155

B.6	The details of the potential, interlayer tunnelling matrices and the band structures with corrugation effects	157
B.7	Some realistic systems to realize the model Hamiltonian (2) of the chapter-3 at the first iteration of the potential	157
B.7.1	A graphene trilayer system	159
B.7.2	A graphene tetralayer system [323, 324]	161
B.7.3	A trilayer system of dissimilar layers	163
B.8	Discussion on the probability-density plot for of the moiré-fractal wave-functions given in Fig.3.2 and Fig.3.4 of the chapter-3	164
B.9	Calculation of the Hubbard parameters	165
B.10	More on the experimental signatures of moiré fractals	167
C	Commensuration in hBN-encapsulated supermoiré structures and its connection with moiré fractal	168
C.1	Details of parameter space of the supermoiré systems	168
C.1.1	Supermoiré (SM) harmonics	169
C.1.2	Diophantine Equation for commensurate SM structure	170
C.2	The derivation of effective Hamiltonian $H_{\text{eff}}^{(1,2)}$ for hBN-Graphene(BLG)-hBN supermoiré system	171
C.2.1	Evaluation of the Green's function	174
C.3	Generic model Hamiltonian for moiré fractals in strained twisted homobilayers	176
	Author Biodata	178

LIST OF FIGURES

- 1.1 (a) The Brillouin zone (BZ) of the three individual layers superposed over one another, followed by their respective rotations with respect to the middle layer. $K_-^{(\ell)}$ marks the left valley at the BZ corners of layer- ℓ and K_+^ℓ marks the right valley of layer- ℓ . The same flavour valleys are connected through the reciprocal lattice vectors. The black star at the centre marks the high-symmetry Γ -point, while P marks a generic point in the reciprocal space that can be reached from the Γ -point via the three nearest lying K-valleys plus the three vectors \mathbf{k}_1 , \mathbf{k}_2 and \mathbf{k}_3 of each layer. The two small hexagons on the right identify the moiré Brillouin zone corresponding to two moiré interfaces between layer-1/2 and layer-3/2, which are also misoriented w.r.t. each other. (b) and (c) display the moiré fractal for $(q, p) = (3, 1)$ and $(q, p) = (2, 1)$, respectively. The quantity fractal dimension (D_f) is the fractal or Hausdorff dimension. The geometries which are shown below the D_f are the fractal generators corresponding to the (q, p) value. 7
- 2.1 (a) The honeycomb lattice of graphene. The two sublattices are denoted by A (black-points) and B (Gray-points). The two real-space primitive vectors \mathbf{a}_1 and \mathbf{a}_2 are making a unit cell (green rhombus) that contains two atoms of either type A and B. It also shows the three nearest-neighbours vectors δ_1 , δ_2 and δ_3 connecting each nearest B-type atom from a given A-type atom. (b) The full dispersion of the pristine single layer graphene (SLG) using the Hamiltonian (2.19). There are six points (the corners of the first Brillouin zone (FBZ)) where the conduction and valence bands make contact and form a hexagon. In the vicinity of these points, the bands disperse conically, forming the Dirac cones (condensed matter version of light-cone). (c) The energy contour plot of the conduction band. The red hexagon marks the FBZ and also labels the high-symmetry points, Γ : centre of the BZ, K : DP with $\xi = 1$, M : Midpoint of the line-joining the two adjacent corners, K' : DP with $\xi = -1$. In the close vicinity of DPs (K or K'), the shape of the contours are circular and become triangular in shape as one goes away from the DPs (the trigonal warping). 19
- 2.2 (a) Illustrating the M-points in the SLG band structure where the saddle points occur [148]. (b) The density of states for SLG with overlap parameter $s = 0$ (Gray line) and $s = 0.07$ eV (dash-dotted) black line. 23

- 2.3 One-dimensional graphene superlattice (SL) formed by a cosine potential periodic along the x-direction with periodicity $L = 50a$. (a) It shows the full three-dimensional dispersion of the first two conduction bands and valence bands with the new set of DPs at the potential strength $V_0 = 0.4$ eV. (b) It shows the contour plot corresponding to the first conduction band. The Fermi velocity gets renormalized along the y-direction as the potential is applied along the x-axis. (c) It shows the density of states (DOS) plot at three different potentials 0 eV, 0.12 eV and 0.2 eV. 29
- 2.4 (a) One-dimensional graphene SL formed by a symmetric Krönig-Penney-like rectangular-barrier potential periodic along the x-direction with periodicity $L = 50a$. The height of the potential is U_0 , and w is the width of the potential well. (c) It shows the full three-dimensional dispersion of the first two conduction bands and valence bands with the new set of DPs at the potential strength $V_0 = 0.4$ eV. (d) It shows the contour plot corresponding to the first conduction band. The Fermi velocity gets renormalized along the y-direction as the potential is applied along the x-axis. 30
- 2.5 (a) The equi-energy contours plotted using (2.51) for different values of $m = 0, 1, 2$ of the newly generated massless Dirac fermions for cosine potential. For $m = 0$, the blue circle denotes the isotropic Dirac cone. However, as the m increases, the Dirac cones become anisotropic along the y-axis. (b) Same for the Krönig-Penney-like potential. 31
- 2.6 (a) Two-dimensional graphene SL formed by a muffin-tin *square* potential periodic along the x- and y-direction with translation vector $T(n_1, n_2) = n_1 L \hat{x} + n_2 L \hat{y}$. The height of the potential barrier is U_0 inside the circular regions of radius w and zero outside. The adjacent right figure shows the corresponding reciprocal space where the blue square indicates the SL Brillouin zone (SBZ). (b) The difference of the energy (ΔE) between the first two conduction bands above the Fermi level is plotted against the path $M'_{SBZ}, X_{SBZ}, M_{SBZ}$. (c) It shows the three-dimensional (3D) view of the first two conduction bands with the new set of eight DPs occurring at $G = \pm G_1/2, G = \pm G_2/2$ and at the corners of the SBZ. (d) It shows the contour plots corresponding to the first conduction band with elliptical contours indicating the modified Fermi velocity of new DPs. (e) It shows the density of states with two symmetrically placed dips. 32

- 2.7 (a) two-dimensional (2D) graphene SL formed by a muffin-tin *hexagonal* potential periodic along the x- and y-direction with translation vector $\mathbf{T}(n_1, n_2) = (n_1 + n_2/2)L\hat{x} + (\sqrt{3}n_2/2)L\hat{y}$. The height of the potential barrier is U_0 inside the circular regions of radius w and zero outside. The adjacent right figure shows the corresponding reciprocal space where the blue hexagon marks the SBZ. (b) The difference of the energy (ΔE) between the first two conduction bands above the Fermi level is plotted against the path $K_{SBZ}, M_{SBZ}, K'_{SBZ}$. (c) It shows the 3D view of the first two conduction bands with the new set of six DPs occurring at $\mathbf{G} = \pm\mathbf{G}_1/2$, $\mathbf{G} = \pm\mathbf{G}_2/2$ and $\mathbf{G} = \pm(\mathbf{G}_1 + \mathbf{G}_2)/2$. (d) It shows the contour plots corresponding to the first conduction band with elliptical contours indicating the modified Fermi velocity of new DPs. (e) It shows the DOS with two symmetrically placed dips. 33
- 2.8 (a) The schematic of the moiré pattern in Graphene/hexagonal Boron Nitride (G-hBN) at the rotation angle of 8° . (b) The left y-axis shows the variation of moiré wavelength with the relative rotation angle θ , and the right y-axis shows the relative misorientation of moiré pattern with the graphene layer. (c) It shows the reciprocal space BZ of SLG (Dark green), hexagonal Boron Nitride (hBN) (Gray) and the BZ corresponding to moiré primitive vectors. (d) The 3D band structure of G-hBN clearly shows the SL DPs in addition to the DP at zero energy. (e) A contour plot where the elliptical-shaped yellow contours clearly indicate the SL DPs with modified Fermi velocity perpendicular to the reciprocal lattice vectors $\mathbf{b}_1^M, \mathbf{b}_2^M$ and $\mathbf{b}_1^M + \mathbf{b}_2^M$. (f) It shows the DOS plot for two different strengths of potentials $V_0 = 0.25$ eV and $V_0 = 0.4$ eV at the angle $\theta = 4^\circ$. The two symmetrically placed dips on either side of the Fermi level indicate the occurrence of SL DPs. 37
- 2.9 A real space moiré-pattern in twisted bilayer graphene (tBLG) at (a) $\theta = 5^\circ$ and (b) $\theta = 5.086^\circ$. The moiré primitive vectors \mathbf{a}_1^M and \mathbf{a}_2^M are shown by black arrows. The black hexagon is formed by connecting AA-rich regions and forms the moiré unit cell, and $L_M = |\mathbf{a}_1^M| = |\mathbf{a}_2^M|$ is the corresponding side length of the hexagon referred to as the *moiré period* or *moiré wavelength*. The two vectors \mathbf{r}_A and \mathbf{r}_B are connecting the centre of the moiré cell to the local AB and BA-stacking regions, respectively. (c) The variation of moiré period L_M with the twist angle θ . Ideally, $L_M \rightarrow \infty$ for $\theta \rightarrow 0$ in tBLG, but here the finite period close to $\theta = 0$ is due to the chosen points on the θ -axis. 39

- 2.10 (a) AA-stacked bilayer graphene. (b) AB- or Bernal-stacked bilayer graphene (BLG). (c) The band structure is plotted along the x-axis and passes through both the valleys \mathbf{K}' (left grey dashed line parallel to the y-axis) and \mathbf{K} (right Gray dashed line). The inset shows the zoom-in of the bands near the \mathbf{K} -valley. 41
- 2.11 The ellipse generated by the equation $3x^2 + y^2 = 1$. Only those points for which $x, y \in \mathbb{Q}^+$ are allowed solutions. 42
- 2.12 (a) Commensurate tBLG at $\theta = 13.1736^\circ$. The two black arrows mark the primitive lattice vectors \mathbf{a}_1^c and \mathbf{a}_2^c of the commensurate structure and the corresponding unit cell is shown by the rhombus. This commensurate structure is SE-even. (b) The commensuration pair at twist angle $\theta = 46.8264^\circ$. The primitive lattice vectors are \mathbf{a}_1^c and \mathbf{a}_2^c . This commensurate structure is SE-odd. 45
- 2.13 The red and blue hexagons show the BZ of two rotated SLG at $-\frac{\theta}{2}$ and $\frac{\theta}{2}$, respectively. The two vectors $\mathbf{K}^{\frac{\theta}{2}}$ and $\mathbf{K}^{-\frac{\theta}{2}}$ points the corresponding DPs at the right valley $\xi = 1$ and the vector $\Delta\mathbf{K} = \mathbf{K}^{\frac{\theta}{2}} - \mathbf{K}^{-\frac{\theta}{2}}$ points the shift between them. The two primitive reciprocal space lattice vectors corresponding to the real-space commensurate tBLG are \mathbf{b}_1^c and \mathbf{b}_2^c such that $\mathbf{a}_i^c \cdot \mathbf{b}_j^c = 2\pi\delta_{ij}$ for $i, j = 1, 2$ and the black hexagon centred at the middle point of $\Delta\mathbf{K}$ shows the BZ of the real space commensurate tBLG. 47
- 2.14 (a) The band structure along the y-axis passing through both the DPs at $\pm\Delta\mathbf{K}/2$ at twist angles 3.89° and 1.79° . (b) The band structure along the x-axis passes through through the DP at $\Delta\mathbf{K}/2$ at twist angles 3.89° and 1.79° . (c)-(d) The 3D band structures showing the first valence and conduction bands at $\theta = 1.79^\circ$ and $\theta = 3.89^\circ$, respectively. (e) The DOS for two angles at $\theta = 3.89^\circ$ and $\theta = 1.79^\circ$. The red dashed lines parallel to the y-axis mark the Van Hove singularity (VHS) for twist angle 1.79° and the dashed red lines in the inset mark the maximum of the conduction band (saddle point) and minimum of the valence band (saddle point) where the VHSs occur. (f) The figure shows the renormalized Fermi velocity for the commensurate tBLG at different commensurate angles. For very small angles, the quantity $\frac{\tilde{v}_F}{v_F \Delta K}$ is no longer small and the perturbation theory breaks down. 49
- 2.15 (a) The figure shows layer 1 (red) and layer 2 (blue) with different primitive lattice vectors stacked over one another. (b) The figure shows the projection of the atom \bar{X} (blue) of an arbitrarily chosen cell of layer 2 on layer 1. Also, the in-plane distance $\mathbf{r} = \mathbf{R}_{\bar{X}} - \mathbf{R}_X - d\hat{z}$ (green) between the atom X (red) of a cell of layer 1 and atom \bar{X} . 52

- 2.16 It shows the rapid decay of the Fourier amplitude t_q of the interlayer coupling. The black solid line is plotted for the functional form of $V_{pp\pi}$ and $V_{pp\sigma}$ given in [253], while the black (dashed-dot) line shows the plot for ansatz in (2.121). The vertical dashed grey line parallel to the y-axis crosses the x-axis at $K_D a_0 = 4\pi/3\sqrt{3}$. 58
- 2.17 (a) It shows the BZ of individual layers (red and blue) and the reciprocal lattice vectors for both layers. The vectors $\mathbf{b}_1^M = \mathbf{b}_1^{-\theta/2} - \mathbf{b}_1^{\theta/2}$ and $\mathbf{b}_2^M = \mathbf{b}_2^{-\theta/2} - \mathbf{b}_2^{\theta/2}$ are the moiré reciprocal lattice vectors. $\mathbf{q}_1, \mathbf{q}_2$ and \mathbf{q}_3 connects the DPs of one layer to another. (b) The moiré Brillouin zone (mBZ) created for the momenta states such that their magnitude is less than $2\mathbf{b}_1^M$. (c) The mBZ for the momenta states with magnitude is less than $4\mathbf{b}_1^M$. 59
- 2.18 (Top) The Band structure of tBLG is plotted against the high-symmetry path $\tilde{K}' \rightarrow \tilde{K} \rightarrow \tilde{\Gamma} \rightarrow \tilde{\Gamma} \rightarrow \tilde{K}'$ at twist angles $\theta = 5^\circ$, $\theta = 1.05^\circ$ and $\theta = 0.5^\circ$. The interlayer hopping amplitude $w_{AA} = \tilde{t}(\mathbf{q})/\Omega$ in AA-rich region and $w_{AB} = \tilde{t}(\mathbf{q})/\Omega$ in AB-rich region are considered identical and is equal to 110 meV [11]. The Gray dashed line at $E = 0$ is the Fermi level, and the two bands nearest to the Fermi level are shown in solid black lines. (Bottom) The Band structure of tBLG is plotted against the same high-symmetry path as in the top figure at twist angles $\theta = 5^\circ$, $\theta = 1.05^\circ$ and $\theta = 0.5^\circ$. The interlayer hopping amplitude $w_{AA} = \tilde{t}(\mathbf{q})/\Omega$ in AA-rich region and $w_{AB} = \tilde{t}(\mathbf{q})/\Omega$ in AB-rich region are considered to be different and are equal to $w_{AA} = 79.7$ meV and $w_{AB} = 97.5$ meV. [254] 61
- 2.19 (a) It shows the DOS plot for tBLG at twist angle $\theta = 5^\circ$. The locations of the VHS are marked using red dashed lines parallel to the y-axis. (a) The DOS plot at the first magic angle $\theta = 1.05^\circ$. The locations of VHS are marked using red dashed lines parallel to the y-axis. 62
- 2.20 (a) Band structure of tBLG without the interlayer coupling in AA-rich regions at twist angle $\theta = 5^\circ$. The dashed grey line marks the Fermi level, and the two solid black lines show the two lowest bands, which are isolated from the higher bands. (b) The band structure at the first largest magic angle of approximately $\theta = 1.086^\circ$. The two lowest bands form the perfectly flat bands. (c) The band structure at the second magic angle of approximately $\theta = 0.29^\circ$. 67

- 3.1 (a) L_N , β and x over triangular coordinates (the axes are 60° with respect to each other). The intersection of β (magenta)- and x (green)-lines identify the intersection points $(x, y = x + \beta)$ at which L_N exists. (b) The real-space creation of each iteration: tBLG is created by stacking graphene layers, with the top layer being the zeroth iteration $j = 0$ and the bottom layer being the next $j = 1$. The iterations $j = 2, 3, \dots$ are created by applying the z -independent external periodic potentials identically to both the graphene layers. (c) The $K = 3$ CPT hierarchy (since a hexagon of each layer encloses three hexagons of an adjacent layer), where each layer corresponds to a particular order of settlement [284]. L_N is analogous to K . 77
- 3.2 (a1), (b1) The BZ for $j = 1$ (black), 2 (magenta) 3 (green), where $\{b_1^{(1)}, b_2^{(1)}\}$ are the reciprocal lattice primitive vectors for $j = 1$. (a2), (b2) The fractal structures at the BZ edges. The dashed red hexagon represents the initiator, *i.e.*, the BZ of SLG rotated by $\theta/2$. The solid blue lines outline the fractal structures' outer boundary. The generators (inside) attach alternately to the initiator, forming the fractal structure. The copies of the BZ at each iteration are added such that they overlap with the BZ of SLG (red solid line in (a1, b1)), and these overlaps lead to IFs. The insets between (a1), (a2) and (b1), (b2) display reciprocal and real-space lattice vectors for $q = 3, p = 1$ and $q = 2, p = 1$, respectively. The shift between the Dirac points is equal to the hexagon's side length for $q = 3, p = 1$, and twice its side for $q = 2, p = 1$. (a3) and (b3) The band structures for $V_0 = 1.2$ meV and the DOS (with a Gaussian smearing of 0.002 meV). (a4) and (b4) show $\rho_{nk}(\mathbf{r})$ of the lowest conduction band (dashed-dotted line) at the Dirac point (see text, Appendix-B.8). 78
- 3.3 $\Delta A/A_{\text{FBZ}}^{(j-1)}$ vs. θ : the blue rectangles represent commensurate/closest angles for odd q and $p = 1$. The first BZ area for incommensurate angles is determined using moiré vectors[254]. The inset confirms the absence of the apparent multivaluedness in the lowest values of the V-regions between the dashed lines, with a separation of $\sim 0.002^\circ$. 81

3.4 The band structures at $\theta_r \sim 21.79^\circ$ in (a) and $\theta_r \sim 13.17^\circ$ in (b) along $K' - M - \Gamma - K$. The twist between the layers is the first magic angle $\theta \sim 1.05^\circ$. The interlayer hopping parameters: $t_{AA/BB} = t_{AB/BA} = 110$ meV (Appendix-B.6) and $V_0 = 1.2$ meV. (left to right) The emergent fractal structure in reciprocal space, 2D-band structure: orange (blue) bands without (with) moiré external potential (mEP), the DOS, and the spatial profiles of $\rho_K(\mathbf{r})$ of the lowest conduction band with $j = 2$, where the solid black line shows the Wigner-Seitz (WS) cell. Changing θ_r from (b) to (a) modifies D_f , shifting more bands towards E_F .

83

4.1 (a) The BZ of the three individual layers superposed over one another, followed by their respective rotations with respect to the middle layer. $K_-^{(\ell)}$ marks the left valley at the BZ corners of layer- ℓ and $K_+^{(\ell)}$ marks the right valley of layer- ℓ . The same flavour valleys are connected through the reciprocal lattice vectors such that the two vectors $\mathbf{b}_1^{(1)} - \mathbf{b}_2^{(1)}$ and $\mathbf{b}_1^{(3)} - \mathbf{b}_2^{(3)}$ connect the right valley of layer-1 and layer-3. The black star at the centre marks the high-symmetry Γ -point, while P marks a generic point in the RS that can be reached from the Γ -point via the three nearest lying K -valleys plus the three vectors \mathbf{k}_1 , \mathbf{k}_2 and \mathbf{k}_3 of each layer. The two small hexagons on the right identify the moiré BZ corresponding to two moiré interfaces between layer-1/2 and layer-3/2, which are also misoriented with respect to each other. (b1) The variation of the second-order moiré length is plotted against $\theta_{12} \in [1^\circ, 5^\circ]$ for a fixed angle $\theta_{32} = 2.8^\circ$ and the blue stars mark the various possible commensurations of around 2.8° (see text). (b2) The maximum second-order moiré length scale of two moiré interfaces is plotted by considering the range of angles $\theta_{12} = -\theta_{32} \in [-5^\circ, 5^\circ]$. This pattern is diagonally-symmetric about the diagonal $\theta_{23} = -\theta_{12}$. (c1), (c2) The same geometrical analysis is performed with a non-vanishing lattice mismatch $\delta = 0.018$, particularly depicting the hBN-encapsulated single-layer and bilayer configurations. (d) In this work, we are interested in the part of the parameter space where the moiré-patterns in two-layer interfaces make a commensurate angle with each other. Therefore, this geometry shows two moiré BZ (maroon and dark blue) of equal side length and the commensurate mini BZ (black) at $(q, p) = (3, 1)$. The outer boundary of the mini BZ overlapping either of the mBZ provides a shape that can be generated using a generator [82, 281, 328].

88

- 4.2 (a) Structures leading to the effective Hamiltonian of an AAA-stacked hBN-encapsulated single-layer graphene and an AAA-stacked hBN-encapsulated Bernal-stacked bilayer graphene. The layers are indexed in both configurations using $\ell = 1, 2, 3$ from the top to bottom. The potentials $U^{(21)}$, $U^{(23)}$, and $U^{(34)}$ show a visual representation of the Eqs. B.21 and 4.5. The moiré fractal corresponding to $(q, p) = (3, 1)$ for both the cases *viz.* hBN-encapsulated SLG and hBN-encapsulated BLG is identical to Fig. 4.1(d) where the two solid lines in maroon and dark blue represent the BZ of both the hBN layers and the black solid line represents the seven copies of the BZ of the supermoiré configuration. (b) The pseudocolor spatial distribution of the functions $g_1(\mathbf{r})$ and $g_2(\mathbf{r})$ in both the top and bottom moiré interfaces. In the top row, the $g_1(\mathbf{r})$ and $g_2(\mathbf{r})$ of the top moiré interface are rotated anticlockwise, while the $g_1(\mathbf{r})$ and $g_2(\mathbf{r})$ of the bottom moiré interface are rotated clockwise. The PV in both the moiré interfaces are shown by black arrows. (c1) and (c2) show the bandstructures and density of states that correspond to hBN-Graphene-hBN for $(q, p) = (3, 1)$ and hBN-BLG-hBN also for $(q, p) = (3, 1)$, respectively. In both cases, the number of bands within the gap of the lowest-four bands (with valley degeneracy) remains identically $4(e^{2\ln(n_c)/L_N} - 1)$, where L_N is a L schian number [304, 328, 371].
- 4.3 Isoenergy ARPES contour momentum distributions for (a) relaxed magic-angle twisted bilayer graphene and (b) graphene-hBN interface with a strained graphene layer closer to hBN at different photoelectron energy with x - and y -polarized light states. The colour bar shows the ARPES intensity obtained with x - and y -polarization states of light in $I(\mathbf{p}, E)$ with a Gaussian smearing factor 0.02. The top rows show the right-valley bandstructure along the high-symmetry path, which is also indicated in the BZ adjacent to the bandstructure plots. The dashed line below the E_f in the valence band region marks the energy levels at which the ARPES intensity calculation is performed. These lines are also indicative of the ARPES contour features, *e.g.*, the dashed lines in (a) crossing the bands only near the Γ -point and therefore, the ARPES contribution comes from the region around the Γ -point. Similarly, the ARPES contribution in the case of G-hBN moir  interface at different levels of energy shift from the K' -point to the corners of the BZ. The colourmaps are drawn using a power norm with exponent 1.1.

91

93

- 4.4 Top panel: (a) and (b) show the isoenergetic ARPES contour momentum distributions for hBN-encapsulated single-layer graphene for different photoelectron energies with x - and y -polarized light states for $(q, p) = (3, 1)$. The white dashed lines show the BZs of the moiré-patterns in two interfaces, and the solid white line shows the BZ of the resulting commensurate supermoiré structure. The star at the centre represents the high-symmetry Γ -point. The ARPES intensities are calculated using a Gaussian smearing factor of 0.005. (c),(d) show the tunneling current (I_t) in hBN-encapsulated SLG corresponding to two different supermoiré commensurations $(q, p) = (3, 1)$ and $(q, p) = (5, 1)$ respectively. The bias voltage in the current calculation is set to be $V_{\text{bias}} = -0.15$ V. The two vectors $\mathbf{a}_1^{(2)}, \mathbf{a}_2^{(2)}$ show the primitive lattice vectors in the supermoiré structures and the number of peaks that resonates with the predicted precounted number of bands count is marked in black. Bottom panel: A similar analysis is performed for the hBN encapsulated bilayer graphene (hBN-BLG-hBN). The only difference is the bias voltage $V_{\text{bias}} = -0.1$ V. 96
- B.1 (a) The stepwise creation of the FG for $L_N = 7$ with $q = 3$ and $p = 1$, and (b) $L_N = 13$ with $q = 2$ and $p = 1$. The red dashed line is the side \mathbf{u} of A_0 as defined in the Sec. B.1 151
- B.2 (a) The fractal corresponding to one more entry in the Table-B.1 where $q = 11$ and $p = 3$ having $L_N = 31$ with $\beta = 4$ at an angle of $\theta_r = 17.89^\circ$ for $j = 1, 2$. (b) the fractal corresponding to the iteration $j = 3$. 152
- B.3 (a) The real-space structure of commensurate tBLG at $\theta \sim 21.79^\circ$ and two levels of periodic potentials for $j = 2, 3$. The direct-lattice primitive vectors are also shown for each level. (b) The corresponding moiré fractal (MF) along the edges of the Wigner-Seitz unit-cell at $j = 3$. (c) The initiator, the arm of the hexagon corresponding to $j = 3$, and the FG. 153
- B.4 p_1 vs p_2 for two maximum values of q . Evidently, the points arrange themselves in hexagons, and each point is associated with a L schian number L_N . 154
- B.5 The inclusion of corrugation effects leads to different interlayer hopping parameters, namely, $t_{AA, BB} = 79.7$ meV and $t_{AB, BA} = 97.5$ meV [254]. This does not change the $2e^{2\ln(n_c)/D_f} - 2$ bands inserted within the band-gap of the two lowest bands at the Γ -point (shown by the two arrows) in the absence of mEP and hence the corrugated tBLG also does not affect the emergence of fractality. 156

- B.6 (a) The renormalized Fermi velocity v_F^*/v_F as a function of α^2 and hence the twist angle θ . (b) The Fermi energy (E_F) as a function of α^2 . Similar to the case of a pristine tBLG [11] or an unrotated mEP to tBLG [78], the renormalized Fermi velocity in the presence of a rotated mEP remains unaffected both in the absence and the presence of the corrugation effect. 156
- B.7 A (a) trilayer-, (b) a four-layer-twisted graphene, and (c) a trilayer boron nitride-Graphene-boron nitride system. In the above ● denote carbon, ● boron and ● nitrogen atoms, respectively. The angle θ_r is one of the commensurate angles and $d_0 \sim 0.335$ nm is the interlayer separation in tBLG. The number beside each layer represents the layer index used in the text in appendix- B.8. 158
- B.8 (a) The spatial variation of the inversion symmetry preserving part $V^{\text{eff}}(\mathbf{r})$, where the color bar is in the units of t_0^2/V_{STM} , and (b) the spatial variation of the mass-dependent term $M_{11}^{\text{eff}}(\mathbf{r})$ that breaks the inversion symmetry. Here the color bar is in the units of $\sqrt{3}t_0^2/V_{\text{STM}}$. 159
- B.9 The band structure corresponding to the trilayer graphene system with increasing values of the interlayer bias voltage (a) $V_{\text{STM}} = 10$ meV, and (b) $V_{\text{STM}} = 40$ meV. The solid orange lines show the band structure in the absence of the potential while the blue lines represent the eigenvalues of $H_2(\mathbf{r})$ without the perturbation, while the cyan lines show the band structure of $H_2(\mathbf{r}) + H_{\text{pert}}(\mathbf{r})$ calculated upto the first order in perturbation. The dotted cyan lines show $4e^{2\ln(n_c)/D_f} - 2$ bands within the bandgap of the lowest two bands at the Γ -point. 161
- B.10 The band structure of the tetralayer graphene system as shown in Fig. B.7(b) for $V_{\text{STM}} = 20$ meV. The solid orange lines show the band structure in the absence of the potential while the blue lines represent the eigenvalues of $H_2(\mathbf{r})$ without the perturbation, while the cyan lines show the band structure of $H_2(\mathbf{r}) + H_{\text{pert}}(\mathbf{r})$ calculated up to the first order in perturbation. The dotted cyan lines show $4e^{2\ln(n_c)/D_f} - 2$ bands within the bandgap of the lowest two bands at the Γ -point. 162

- B.11 (a) The two blue and dashed blue hexagons show the moiré **BZ** of the top and bottom moiré interfaces for the trilayer hBN encapsulated single layer graphene (**hBN-G-hBN**) shown in Fig. B.7(c). The inner red hexagon is the supermoiré (**SM**) **BZ**. (b) The band structures for two different values of q, p along the high-symmetry path X - Y - K - X [87] as shown in (b). The solid blue lines show the band structures of the **G-hBN** system with $V_2(\mathbf{r}) = 0$ while the solid red lines represent graphene sandwiched between two **hBN** layers as in Fig. B.7(c). The two dark grey arrows show the bandgap between the two lowest bands at the Y -point where the $2e^{2\ln(n_c)/D_f} - 1$ bands are inserted. 164
- B.12 The bandwidth of the conduction and valence band in the presence of **mEP** for $q = 3, p = 1$ for (a) $t_{AA, BB} = t_{AB, BA} = 110$ meV [11], and (b) $t_{AA, BB} = 79.7$ meV and $t_{AB, BA} = 97.5$ meV [101, 254]. The bandwidth t_w is in the unit of t_{w0} , which is the bandwidth of pristine **tBLG** at $\theta \sim 1.05^\circ$. 165
- C.1 The band structures for moiré fractals with the (a) 1st shell only, (b) 1st and 2nd shell only and (c) up to 3rd shell for the magic-angle twisted bilayer graphene (**MATBLG**) with $\theta = 1.05^\circ$ and $\theta_r(3, 1) = 21.79^\circ$. The solid lines represent the right valley $\xi = 1$, and the dashed lines represent the left valley $\xi = -1$. For all shells, the number of bands within the gap of lowest-four bands (with valley degeneracy) remains identically $4(e^{\ln(n_c)/L_N} - 1)$. 176

LIST OF TABLES

2.1	Tabulates the different quantities with their corresponding expression for a one-dimensional (1D) cosine potential and a 1D KP potential.	28
2.2	The most dominant Fourier amplitudes for (2.88).	50
2.3	The most dominant Fourier amplitudes for the Bernal-stacked BLG where $\phi = 2\pi/3$. $T^{\alpha\beta}(\mathbf{q})$ is defined in the text.	60
4.1	The parameters in the effective Hamiltonian of Eq.4.6 in the presence of the lattice relaxation. All numbers are in meV [374].	95
B.1	Each commensuration is characterized uniquely by a pair of coprime-integers (q, p) . The L�schian number L_N and the FG are obtained by identifying the number of sides n_c in the FG. The fractal dimension (D_f) corresponding to the various q, p are calculated using L_N and n_c [371]. The outer boundary of the mini-zones superposed over the FBZ of SLG is generated by attaching the FG to a hexagonal initiator.	151
B.2	Explicit form of H_{pert} for trilayer and tetralayer graphene systems after ignoring the vector potential term. The quantities \mathcal{I}_2 is the second order identity matrix, and σ_z is z component of the Pauli matrix. $V^S(\mathbf{r})$ in (B.15) consists of various moir� potentials V_{ij}^{eff} between the layers. The integer subscripts ij in different terms appeared above refer to the layer indices as indicated in Fig. B.7. The detailed expressions for various terms in H_{pert} each SM system are given in the text.	158
C.1	Linear mappings \mathcal{L}_1 , \mathcal{L}_2 and \mathcal{L}_M for various cases.	168

LIST OF SYMBOLS

\mathbb{N} The natural numbers

\mathbb{Z} The integer numbers

\mathbb{Q} The rational numbers

\mathbb{R} The real numbers

\mathbb{C} The complex numbers

\in Set membership

\mathbb{R}^n Space of n -tuples of real numbers

$\|x\|$ Norm of a vector x

LIST OF ACRONYMS/ ABBREVIATIONS

- 1D** one-dimensional
- 2D** two-dimensional
- 3D** three-dimensional
- SLG** single layer graphene
- hBN** hexagonal Boron Nitride
- BLG** bilayer graphene
- BZ** Brillouin zone
- FBZ** first Brillouin zone
- DOS** density of states
- VHS** Van Hove singularity
- SL** superlattice
- mBZ** moiré Brillouin zone
- tBLG** twisted bilayer graphene
- MATBLG** magic-angle twisted bilayer graphene
- vdW** van der Waals
- MF** moiré fractal
- tDBG** twisted double bilayer graphene
- tTLG** twisted trilayer graphene
- TMD** transition metal dichalcogenide
- G-G** Graphene/Graphene
- mEP** moiré external potential
- G-hBN** Graphene/hexagonal Boron Nitride
- D_f fractal dimension

hBN-G-hBN hBN encapsulated single layer graphene

hBN-BLG-hBN hBN encapsulated bilayer graphene

SM supermoiré

SMS supermoiré structure